A Novel Surface Registration Algorithm With Biomedical Modeling Applications

Heng Huang, *Member, IEEE*, Li Shen, *Member, IEEE*, Rong Zhang, Fillia Makedon, Andrew Saykin, and Justin Pearlman

***Abstract*—In this paper, we propose a novel surface matching algorithm for arbitrarily shaped but simply connected 3-D objects. The spherical harmonic (SPHARM) method is used to describe these 3-D objects, and a novel surface registration approach is presented. The proposed technique is applied to various applications of medical image analysis. The results are compared with those using the traditional method, in which the first-order ellipsoid is used for establishing surface correspondence and aligning objects. In these applications, our surface alignment method is demonstrated to be more accurate and flexible than the traditional approach. This is due in large part to the fact that a new surface parameterization is generated by a shortcut that employs a useful rotational property of spherical harmonic basis functions for a fast implementation. In order to achieve a suitable computational speed for practical applications, we propose a fast alignment algorithm that improves computational complexity of the new surface registration method from O(n^3) to O(n^2).**

***Index Terms*—Cardiac modeling, medical image computing, spherical harmonics, surface alignment (matching), surface registration.**

I. Introduction

SHAPE modeling and surface representation combine physical measurement of objects with the mathematical model and are important in a large number of scientific and engineering areas. Medical image computing is one of the most important applications. A variety of 3-D modeling techniques are now available for modeling and inspecting the anatomic structures in the diagnosis and treatment of disease. Based on certain mathematical properties (orthogonality, completeness, ordering in spatial frequency, etc.), the spherical harmonics approach provides 3-D models to derive functional information analysis and classify different pathological symptoms, and has been used for the representation of shapes in many types of biomedical image data.

A number of previous spherical-harmonic-based shape descriptions have been developed for medical image computing. Chen *et al*. [1] used this method to model and analyze left ventricular shape and motion. Matheny and Goldgof [2] used 3-D and 4-D surface harmonics to reconstruct rigid and nonrigid shapes. Since all their approaches started from an initial radial surface function $r(\theta, \phi)$, their method was capable of representing only star-shaped or convex objects without holes. Brechbühler *et al*. [3] presented the SPHARM description that is an extended spherical harmonic method for modeling any simply connected 3-D object. The object surface is represented as $v(\theta, \phi) = (x(\theta, \phi), y(\theta, \phi), z(\theta, \phi))^T$ and spherical harmonics expansion is used for all three coordinates. Styner and Gerig [4] and Gerig and Styner [5] applied the SPHARM description technique to perform segmentation and structural analysis on brain tissues. It has also been used for shape modeling and functional analysis for cardiac MRI [6].

Medical applications often require the comparison between different 3-D models. A shape registration step is often necessary for aligning these models together and extracting their shape descriptors (i.e., excluding translation, rotation, and scaling). Like the shape registration using iterative closest point (ICP) algorithm [7], two important substeps are involved in aligning SPHARM models: 1) creating surface correspondence and 2) minimizing the distance between the corresponding surface parts. Once the surface correspondence is established, the distance minimization becomes relatively easy. Thus, the focus of this paper is on creating surface correspondence for two 3-D SPHARM models.

In the past, the first-order-ellipsoid-based method was used for SPHARM shape registration [4], [5]. In this method, the parameter net on the first-order ellipsoid is rotated to a canonical position such that the north pole is at one end of the longest main axis, and the crossing point of the zero meridian and the equator is at one end of the shortest main axis. The aligned parameter space creates surface correspondence between two models: two points with the same parameter pair (θ, ϕ) on two surfaces are defined to be a corresponding pair. This alignment technique works only if the first-order ellipsoid is a real ellipsoid, as in the case of hippocampal data [5], but not if it is an ellipsoid of revolution or a sphere. There are also many other cases in which this first-order-ellipsoid-based alignment method may not work. We give one example of cardiac ventricle in Fig. 3 as a failed case using this method.

Problems associated with the first-order ellipsoid method and the need for better shape modeling and analysis in current medical applications encouraged this research work. Instead of aligning the first-order ellipsoid, we employ a more general metric for establishing surface correspondence: minimizing the mean squared distance between two SPHARM surfaces. The idea is to fix one object and rotate the mesh of the other one to find

Manuscript received October 19, 2005; revised April 17, 2006.

H. Huang and F. Makedon are with the Department of Computer Science and Engineering, University of Texas at Arlington, Arlington, TX 76019 USA (e-mail: heng@uta.edu).

L. Shen is with the Department of Computer and Information Science, University of Massachusetts Dartmouth, North Dartmouth, MA 02747 USA.

R. Zhang is with the Department of Computer Science, Dartmouth College, Hanover, NH 03755 USA.

A. Saykin is with the Department of Radiology, Indiana University School of Medicine, Indianapolis, IN 46202 USA.

J. Pearlman is with the Department of Cardiology and Radiology, Dartmouth Medical School, Lebanon, NH 03756 USA.

Digital Object Identifier 10.1109/TITB.2006.897577

the position with minimum surface distance. When the mesh of an object is rotated, a reparameterization process must be performed to calculate the new SPHARM coefficients. But the standard recalculation [3] (e.g., generating and solving a set of linear equations) of SPHARM coefficients for a reparameterized object is time consuming.

In this paper, based on the rotational properties of harmonics analysis, we prove that a new set of SPHARM coefficients after a rotated parameterization can be directly generated from the original set. Thus, we can easily obtain a new SPHARM model for a reparameterized object by rotating its parameterization along the surface. This process is more explicit and faster than the standard method, because we need not regenerate (redistribute (θ, ϕ) for each sampling points that created the linear equations) and solve the linear equations. Meanwhile, a fast surface alignment algorithm is proposed with the new parameterization method to do the global surface registration. Some medical image computing applications are used to demonstrate our algorithm in this paper.

The closest approach to ours is that of Burel and Hennocq [8], which focused on determining the orientation of 3-D objects without point correspondence information. Their approach applies only to star-shaped objects and their aim is to align the orientation of these objects. Their work can be replaced by aligning two first-order ellipsoids referred to before. Our research differs in aligning the surface correspondence for arbitrarily shaped but simply connect objects, rather than fixing the orientation only for star-shaped objects. The contributions of our work are, thus, twofold: 1) a new approach for establishing surface correspondence, with theoretical proofs and justifications and 2) a fast surface alignment algorithm with applications to several problems in medical image computing.

The paper is structured as follows. Section II describes the proposed surface alignment algorithm and a theorem on some rotational property of a SPHARM parameterization. Section III shows experimental results of applying the proposed algorithm to several medical applications. Section IV concludes the paper.

II. Methods

A. SPHARM Surface Description

The SPHARM technique [3] can be used to model arbitrarily shaped, simply connected 3-D objects. An input object surface is assumed to be defined by a square surface parameter mesh converted from an isotropic voxel representation. Fig. 1(a) shows one example of voxel model that is composed of a mesh of square faces based on the exterior voxels of the object. Two steps are involved in converting the object surface to its SPHARM shape description: 1) surface parameterization and 2) SPHARM expansion.

Surface parameterization aims to create a continuous and uniform mapping from the object surface to the surface of a unit sphere. The parameterization is formulated as a constrained optimization problem with the goals of preserving area and topology while minimizing distortions (see [3] for details). The result is a mapping of two spherical coordinates θ and ϕ [$\theta \in [0, \pi]$ is the polar angle and $\phi \in [0, 2\pi)$ is the azimuthal angle,

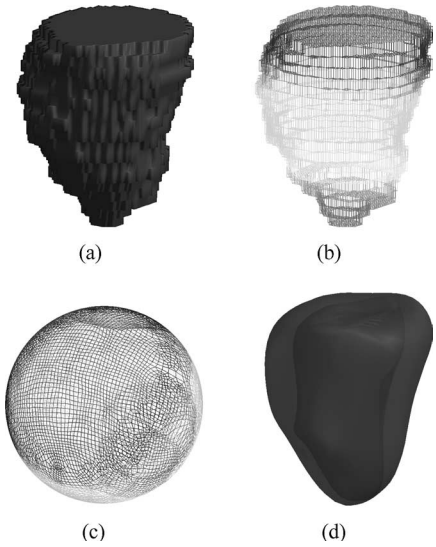

Fig. 1. (a) One example of voxel model that is composed of a mesh of square faces based on the exterior voxels of the object. (b) and (c) Parameterization result of the object surface. During the parameterization procedure, the same color area on the object surface is mapped onto the same color area of the sphere. (d) Reconstructed surfaces of left ventricle, including epicardium and endocardium.

and Fig. 1(b) and (c) shows the parameterization result, where the parameterization aims to preserve the area and minimize the angle distortion] to each point $v(\theta, \phi)$ on a surface

$$v(\theta, \phi) = (x(\theta, \phi), y(\theta, \phi), z(\theta, \phi))^T. \tag{1}$$

When the free variables θ and ϕ range over the whole sphere, $v(\theta, \phi)$ ranges over the whole object surface. *SPHARM expansion* is then used to expand the object surface into a complete set of SPHARM basis functions Y_l^m, where Y_l^m denotes the spherical harmonic of degree l and order m (see [3] for details). The expansion takes the following form:

$$v(\theta, \phi) = \sum_{l=0}^{\infty} \sum_{m=-l}^{l} c_l^m Y_l^m(\theta, \phi) \tag{2}$$

where

$$c_l^m = (c_{lx}^m, c_{ly}^m, c_{lz}^m)^T. \tag{3}$$

The coefficients c_l^m are 3-D vectors. Their components, c_{lx}^m, c_{ly}^m, and c_{lz}^m are usually complex numbers. The coefficients up to a user-desired degree can be estimated by solving a set of linear equations in a least square fashion. The object surface can be reconstructed using these coefficients, and using more coefficients leads to a more detailed reconstruction. Thus, a set of coefficients actually forms an object surface description.

The orthonormality property of spherical harmonic basis functions can be expressed as

$$\int_0^{2\pi} \int_0^{\pi} Y_l^m(\theta, \phi) \bar{Y}_V^m(\theta, \phi) \sin\theta \, d\theta \, d\phi = \delta_{mm'} \delta_W. \tag{4}$$

Here, $\bar{z}$ denotes the complex conjugate and δ_{ij} is the Kronecker delta:

$$\delta_{ij} \equiv \begin{cases} 0, & \text{for} \quad i \neq j \\ 1, & \text{for} \quad i = j \end{cases}.$$

B. Fast Rotation Theorem for Spherical Harmonic Parameterization

According to Euler's rotation theorem, any rotation of the coordinate system (e_1, e_2, e_3) can be decomposed into three elementary rotations $R(\alpha, \beta, \gamma)$: a rotation α around z-axis, which transforms (e_1, e_2, e_3) to (e_1', e_2', e_3'), followed by a rotation β around e_2'-axis, which transforms (e_1', e_2', e_3') to $(\hat{e}_1, e_2', \hat{e}_3)$, and finally, a rotation γ around $\hat{e}_3$-axis. The SO(3) harmonics provide the tool to express the rotated version of a function on the sphere extended by spherical harmonics [9]. The effect of such a rotation on the spherical harmonic basis functions is [10]

$$R_{\mathrm{ZYZ}}(\alpha\beta\gamma)Y_l^m(\theta,\phi) = \sum_{m'=-l}^{l} Y_l^{m'}(\theta,\phi)D_{m'm}^l(\alpha\beta\gamma) \quad (5)$$

where $R_{\mathrm{ZYZ}}(\alpha\beta\gamma)$ represents the rotation operator dependent on the Euler angles; the rotation matrices $D_{m'm}^l(\alpha\beta\gamma)$ [also called the SO(3) matrix elements] are calculated by

$$D_{m'm}^l(\alpha\beta\gamma) = e^{-im'\alpha}d_{m'm}^l(\beta)e^{im\gamma}$$

where

$$\begin{aligned} d_{m'm}^l(\beta) = &\sum_{t=\max(0,m-m')}^{\min(l+m,l-m')} (-1)^t \\ &\times \frac{\sqrt{(l+m)!(l-m!)(l+m')!(l-m')!}}{(l+m-t)!(l-m'-t)!(t+m'-m)!t!} \\ &\times \left(\cos\frac{\beta}{2}\right)^{(2l+m-m'-2t)} \left(\sin\frac{\beta}{2}\right)^{(2t+m'-m)}. \end{aligned}$$

In order to reduce the computations, we use the symmetry properties

$$d_{m'm}^l(\beta) = d_{-m-m'}^l(\beta)$$

and

$$dm'm^l(\beta) = (-1)^{m+m'}d_{mm'}^l(\beta).$$

Since the SPHARM surface modeling technique is employed, the surface coordinate information of a 3-D object is coded onto three unit spheres: an x-sphere, a y-sphere, and a z-sphere. These three spherical functions are expanded using spherical harmonics and are represented by $f(\theta,\phi)(f \in \{x,y,z\})$. We denote $f'(\theta,\phi)$ as the new function after applying a rotation operator $R_{\mathrm{ZYZ}}(\alpha\beta\gamma)$ to $f(\theta,\phi)$ on the f-sphere

$$f'(\theta,\phi) = R_{\mathrm{ZYZ}}(\alpha\beta\gamma)f(\theta,\phi). \quad (6)$$

Thus,

$$v'(\theta,\phi) = \begin{pmatrix} x'(\theta,\phi) \\ y'(\theta,\phi) \\ z'(\theta,\phi) \end{pmatrix} = R_{\mathrm{obj}}(\alpha\beta\gamma) \begin{pmatrix} x(\theta,\phi) \\ y(\theta,\phi) \\ z(\theta,\phi) \end{pmatrix} \quad (7)$$

where

$$R_{\mathrm{obj}}(\alpha\beta\gamma) = \begin{pmatrix} R_{\mathrm{ZYZ}}(\alpha\beta\gamma) & 0 & 0 \\ 0 & R_{\mathrm{ZYZ}}(\alpha\beta\gamma) & 0 \\ 0 & 0 & R_{\mathrm{ZYZ}}(\alpha\beta\gamma) \end{pmatrix}.$$

Then, $v'(\theta,\phi) = R_{\mathrm{obj}}(\alpha\beta\gamma)v(\theta,\phi)$ represents the new parameterization on the surface, which can be generated by rotating the original parameterization along the object's surface about Euler angles (α,β,γ). In other words, the result of applying the rotation matrix $R_{\mathrm{ZYZ}}(\alpha\beta\gamma)$ on the mapping meshes of x-, y-, and z-sphere is to rotate the parameter mesh on the object's surface at the same orientation. Because of the distortions introduced by spherical parameterization, the result of rotation is not identical to the result of applying Euler angles on the sphere, but both will have nearly the same orientation. Thus, we only use R_{obj}, which we refer to as the parametric rotation matrix, for rotating the parameter mesh along the surface of an object. Substituting (2) and (5) into (6) gives

$$\begin{aligned} \sum_{t=0}^{L}\sum_{m=-l}^{l} c_{lf}^m(\alpha\beta\gamma)Y_l^m(\theta,\phi) &= f'(\theta,\phi) \\ &= R_{\mathrm{ZYZ}}(\alpha\beta\gamma)\sum_{l'=0}^{L}\sum_{m'=-l'}^{l'} c_{l'f}^{m'}Y_{l'}^{m'}(\theta,\phi) \\ &= \sum_{l'=0}^{L}\sum_{m'=-l'}^{l'} c_{l'f}^{m'}R_{\mathrm{ZYZ}}(\alpha\beta\gamma)Y_{l'}^{m'}(\theta,\phi) \\ &= \sum_{l'=0}^{L}\sum_{m'=-l'}^{l'} c_{l'f}^{m'}\sum_{n=-l'}^{l'} c_{l'}^n(\theta,\phi)D_{nm'}^{l'}(\alpha,\beta,\gamma) \quad (8) \end{aligned}$$

and multiplying $\bar{Y}_k^j(\theta,\phi)$ on both sides (adjusting k from 0 to L and j from $-k$ to k) and integrating on the sphere. Since all Kronecker delta values are zero except at $k = l = l'$ and $j = m = n$, we get the following:

$$\begin{aligned} c_{lf}^m(\alpha\beta\gamma) &= \sum_{m'=-l'}^{l'} c_{l'f}^{m'}D_{mm'}^{l'}(\alpha\beta\gamma) \\ &= \sum_{m'=-l}^{l} c_{lf}^{m'}D_{mm'}^{l}(\alpha\beta\gamma). \quad (9) \end{aligned}$$

According to this derivation, the harmonics expansion coefficients transform among themselves during rotation. Each new spherical harmonic coefficient $c_{\mathrm{lf}}^m(\alpha\beta\gamma)$ after applying a rotated function $R_{\mathrm{ZYZ}}(\alpha\beta\gamma)$ is a linear combination of the coefficients c_{lf}^m of the original function $f(\theta,\phi)$ $(f \in \{x,y,z\})$. We can use this property to calculate the new SPHARM model $v'(\theta,\phi)$ for the object surface after a rotated parameterization, and we only need the old coefficients $c_{lx}^m, c_{ly}^m, c_{lz}^m$ and rotation matrices $D_{mm'}^l(\alpha\beta\gamma)$.

Theorem (Parameterization Rotation): The parameterization spatial rotation on the surface can be decomposed into three rotations of mapping parameter meshes onto the x-, y-, and z-sphere. $v(\theta,\phi) = \sum_{l=0}^{\infty}\sum_{m=-l}^{l} c_l^m Y_l^m(\theta,\phi)$ represents the parameter mesh of surface. After rotation along the surface in

Euler angles (α, β, γ), the new coefficient $c_{lf}^m(\alpha\beta\gamma)$ is

$$c_l^m(\alpha\beta\gamma) = \sum_{m'=-l}^{l} c_l^{m'} D_{mm'}^l(\alpha\beta\gamma). \tag{10}$$

C. Parameterization Rotation Theorem on Real Spherical Harmonics

Note that the spherical functions used to represent a 3-D surface are functions taking real values. Thus, in some medical imaging applications, real spherical harmonics (RSH) have been used instead of standard (or complex) spherical harmonics to expand these functions.

In order to use RSH to describe simple connected objects (not only for star shape), like the SPHARM technique [3], surface parameterization needs to be performed prior to expansion into harmonics. The expansion takes the following form:

$$v(\theta\phi) = \sum_{t=0}^{\infty} \sum_{m=-l}^{l} c_l^m S_l^m(\theta\phi)$$

where

$$S_l^m(\theta\phi) = \begin{cases} (Y_l^m(\theta\phi) + \bar{Y}_l^m(\theta\phi))/\sqrt{2}, & m > 0 \\ Y_l^0(\theta\phi), & m = 0 \\ -i(Y_l^{-m}(\theta\phi) - \bar{Y}_l^{-m}(\theta\phi))/\sqrt{2}, & m < 0 \end{cases}. \tag{11}$$

The choice of RSH as basis functions in shape modeling requires half the computer memory needed by spherical harmonics. However, they are more difficult to manipulate theoretically, owing to a number of useful relationships that lose their simplicity when stated in terms of the RSH. Thus, in this section, we will extend our theorem to RSH.

Rotational symmetry is preserved under the linear combinations of (11) and the results of RSH can be written as [11]

$$R_{ZYZ}(\alpha\beta\gamma) S_l^m(\theta, \phi) = \sum_{m'=-l}^{l} S_l^{m'}(\theta, \phi) R_{m'm}^l(\alpha\beta\gamma). \tag{12}$$

Since (12) has a form similar to (5) (only using $R_{m'm}^l(\alpha\beta\gamma)$, which is shown in (13), at the bottom of page, to replace the rotation matrices $D_{m'm}^l(\alpha\beta\gamma)$, the proof steps for *parameterization theorem* [(6)–(9)] still hold. As a result, the new coefficients of RSH after rotation can also be calculated by the original coefficients as

$$c_{lf}^m(\alpha\beta\gamma) = \sum_{m'=-l}^{l} c_{lf}^{m'} R_{mm'}^l(\alpha\beta\gamma), \quad f \in \{x, y, z\}. \tag{14}$$

D. Surface Correspondence Difference Measurement

The surface correspondence alignment problem is generally formulated in terms of the optimal parameters, such as (α, β, γ), that minimize some surface distance function. In this paper, we adopt the Euclidean distance as the distance function between surfaces. Formally, for two surfaces given by $v_1(s)$ and $v_2(s)$, we define their distance $D(v_1, v_2)$ as

$$\begin{aligned} D(v_1, v_2) &= \left(\oint \|v_1(s) - v_2(s)\|^2 \, ds \right)^{1/2} \\ &= \left(\oint ((x_1(s) - x_2(s))^2 + (y_1(s) \right. \\ &\quad \left. - y_2(s))^2 + (z_1(s) - z_2(s))^2) \, ds \right)^{1/2} \\ &= \left(\sum_{f \in \{x,y,z\}} \int_0^{2\pi} \int_0^{\pi} (f_1(\theta, \phi) - f_2(\theta, \phi))^2 \right. \\ &\quad \left. \times \sin\theta \, d\theta \, d\phi \right)^{1/2}. \end{aligned} \tag{15}$$

By the orthonormality property of spherical harmonic basis functions (4), the integral

$$\begin{aligned} &\int_0^{2\pi} \int_0^{\pi} f(\theta, \phi)^2 \sin\theta \, d\theta \, d\phi \\ &\quad = \int_0^{2\pi} \int_0^{\pi} \left(\sum_{l=0}^{L} \sum_{m=-l}^{l} c_{lf}^m Y_l^m(\theta, \phi) \sum_{l=0}^{L} \sum_{m=-l}^{l} c_{lf}^m Y_l^m(\theta, \phi) \right) \\ &\qquad \times \sin\theta \, d\theta \, d\phi = \sum_{l=0}^{L} \sum_{m=-1}^{l} (c_{lf}^m)^2 \end{aligned}$$

and

$$\int_0^{2\pi} \int_0^{\pi} f_1(\theta, \phi) f_2(\theta, \phi) \sin\theta \, d\theta \, d\phi = \sum_{l=0}^{L} \sum_{m=-l}^{l} c_{lf_1}^m c_{lf_2}^m.$$

$$R_{m'm}^l = \begin{cases} d_{0m}^l(\beta)\sqrt{2}\cos(m\gamma), & m' = 0, m > 0 \\ d_{m'm}^l(\beta)\cos(m\gamma + m'\alpha) + (-1)^{m'} d_{-m',m}^l(\beta)\cos(m\gamma - m'\alpha), & m' > 0, m > 0 \\ (-1)^{(m'+1)} d'_{m'm}(\beta)\sin(m\gamma + m'\alpha) + d'_{m'm}(\beta)\sin(m\gamma - m'\alpha), & m' = 0, m = 0 \\ d_{00}^l(\beta), & m' < 0, m > 0 \\ d_{m'0}^l(\beta)\sqrt{2}\cos(m'\alpha), & m' > 0, m = 0 \\ (-1)^{m'+1} d_{m'0}^l(\beta)\sqrt{2}\sin(m'\alpha), & m' < 0, m = 0 \\ (-1)^m d_{0m}^l(\beta)\sqrt{2}\sin(m\gamma), & m' = 0, m < 0 \\ (-1)^m d_{-m',m}^l(\beta)\sin(m\gamma - m, \alpha) + (-1)^m d_(m', m)^l(\beta)\sin(m\gamma + m, \alpha), & m' > 0, m < 0 \\ (-1)^{m+m'} d_{m'm}^l(\beta)\cos(m\gamma + m'\alpha) + (-1)^{m+1} d_{m'm}^l(\beta)\cos(m\gamma - m'\alpha), & m' < 0, m < 0 \end{cases} \tag{13}$$

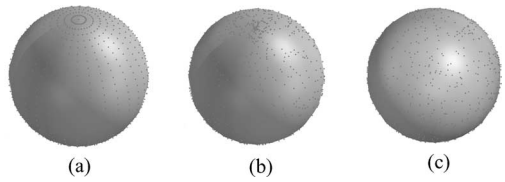

Fig. 2. Sampling methods for searching. (a) Increase Euler angles with equal angular increments step. (b) Simple sampling method with each Euler angle independently, uniformly sampled. (c) Uniform sampling on the surface.

Substituting them into (15) gives the surface difference measure a new form

$$D(v_1, v_2) = \left(\sum_{f\in\{x,y,z\}} \sum_{l=0}^{L} \sum_{m=-l}^{l} \left(c_{lf_1}^m - c_{lf_2}^m \right)^2 \right)^{1/2}. \quad (16)$$

One assumption of this surface correspondence metric is that two object surfaces should be roughly superimposed on each other in the object space. This can be done using the ICP algorithm [7] when necessary.

E. Distance Minimization Algorithm

In this section, we propose an algorithm to determine the rotation that gives the global minimum of (16) and reports the surface correspondence alignment results.

Because we truncate the degree value at $l = L$, the number of spherical harmonics coefficients is $(L+1)^2$. During the distance function minimization procedure, we need to calculate the new parameter mesh coefficients $c_l^m(\alpha\beta\gamma) = (c_{lx}^m(\alpha\beta\gamma), c_{ly}^m(\alpha\beta\gamma), c_{lz}^m(\alpha\beta\gamma))^T$ for every new rotation under Euler angles (α, β, γ). When L is increased, more details of a surface can be obtained, but the computations of new coefficients after rotation will take more time. Because the low-resolution object contributes to the bulk of the shape, it is reasonable to look for the target at low resolution first [11]. In the first step, surfaces reconstructed with $L = 6$ are first used to carry out an approximate minimization of the surface distance function; in a subsequent second step, surfaces reconstructed with $L = 16$ are used to refine the minimization in certain areas determined in the first step.

1) Sampling-Based Search Algorithm: As described earlier, search algorithm proceeds in two steps. In the first step, the straightforward method for minimizing (16) is to fix one parameter mesh and rotate the other to carry out a greedy search on its surface with a small step size. Such an algorithm can finish in O(n^3) time, where n is the sampling number for each Euler angle. For example, in Fig. 2(a), the points on the surface are the north poles' positions in every searching step with angular increments step $2\pi/n$ for α, γ and π/n for β. This method creates more sampling points near the north and south poles and fewer points near the equator, and thus cannot guarantee uniform incremental steps.

A uniform step can improve the efficiency of searching in 3-D configuration spaces. Thus, for efficiency, the rotation space should be first uniformly sampled. In this approach, we sample the surface by calculating a new north pole (n^2 points) and continuing with a counterclockwise rotation around the parameter mesh along the axis between the north and south poles (n steps for every circle).

The simple method might try to uniformly sample each Euler angle independently. However, this cannot derive a uniform point distribution on the surface. In Fig. 2(b) and (c), sets of sampling points on the surfaces of two spheres are visualized to represent the sampling distributions in SO(3) of 900 Euler angles (α, β, γ). Fig. 2(b) shows the result of the simple sampling method. The polar region is oversampled under this method, and accordingly, there are fewer sampling points in the equatorial region.

Fig. 2(c) shows the uniformly distributed sample points generated by a simple and efficient algorithm depicted in Algorithm 1. In this algorithm, we use the random number generator function *r-generator* to return a floating point number in the range [0, 1) and map α into $[0, 2\pi)$, β into $[0, \pi)$, and γ into $[0, 2\pi)$. The inverse sine function of β can avoid oversampling the polar regions. All the sampling points on the surface in Fig. 2(c) are considered as the new north pole. For each candidate north pole, the parameter mesh should be counterclockwise rotated along the north–south axis (the rotation angle ω ranges from 0 to 2π). In order to calculate the coefficients of the new rotated parameter mesh using (10), we must transform the rotation angle ω into the Euler angles (α, β, γ).

Algorithm 1 Uniform Sampling Algorithm for Euler Angles

Initial: the number of sampling points n
Result: uniformly distributed Euler angle rotation set (α, β, γ)
begin
  for $i = 1$ **to** n **do**
    $\alpha_i = 2\pi * r$-generator;
    $\beta_i = \arcsin(1 - 2 * r\text{-generator}) + \pi/2$;
    $\gamma_i = 2\pi * r$-generator;
  end for
  return (α, β, γ)
end

The original north and south poles of a surface's parameter mesh are mapped onto the axis $e_3 = (001)$ and $-e_3 = (00-1)$ in the x-, y-, and z-sphere. After rotation using Euler angles $(\alpha_p, \beta_p, \gamma_p)$, the north and south pole coordinates switch from $v(\theta, \phi)$ to $v'(\theta, \phi) = R_{\text{obj}}(\alpha_p\beta_p\gamma_p)v(\theta, \phi)(\theta = 0 \text{ or } \pi)$. Simultaneously, the axis e_3 in the coordinate systems of the three mapping spheres is changed to $\hat{e}_3 = R_{ZYZ}(\alpha_p\ \beta_p\ \gamma_p)(0\ 0\ 1)^T$. Because $\hat{e}_3$ also contains the origin and has unit length direction, we apply the Rodrigues' rotation formula[1] for computing the rotation matrix $R_{\hat{e}_3} \in \text{SO}(3)$ corresponding to a rotation by an angle ω about the fixed axis $\hat{e}_3$

$$R_{\hat{e}_3}(\omega) = I + S\sin\theta + S^2(1 - \cos\theta)$$

where I is the identity matrix.

[1][Online]. Available: http://mathworld.wolfram.com

We can obtain the Euler angles (α, β, γ) by solving the equation $R_{ZYZ}(\alpha, \beta, \gamma) = R_{\hat{e}_3}(\omega)$. These Euler angles can then be used to calculate the coefficients of new parameter mesh using (10).

Algorithm 2 Sampling-Based Search Algorithm

Initial: SPHARM coefficient sets $\{c_{l1}^m\}$ and $\{c_{l2}^m\}$ and Euler angles set $\{\alpha_i, \beta_i, \gamma_i\}$ generated by Alg. 1
Result: new SPHARM coefficient $\{\hat{c}_{l1}^m\}$
begin
  $D = 10^4$
  $\mathbf{target} = \phi$
  for $i = 1$ to n^2 **do**
    Calculating the new coefficients: $c_{lf}^m(\alpha_i\beta_i\gamma_i) = \sum_{m'=-l}^{l} c_{lf}^{m'} D_{mm'}^l(\alpha_i\beta_i\gamma_i),\ f \in \{x, y, z\}$
    $D_i = (\sum_{f\in\{x,y,z\}} \sum_{l=0}^{L} \sum_{m=-l}^{l} (c_{lf}^m(\alpha_i\beta_i\gamma_i) - c_{lf_2}^m)^2)^{1/2}$
    If $D_i \le D$ **then**
      $D = D_i$
      $\mathbf{target} = \{c_l^m(\alpha_i\beta_i\gamma_i)\}$
    end if
    for $j = 1$ **to** n **do**
      Calculating the new coefficients: $c_{lf}^m(\alpha_{ij}\beta_{ij}\gamma_{ij}) = \sum_{m'=-l}^{l} c_{lf}^{m'}(\alpha_i\beta_i\gamma_i) D_{mm'}^l(\alpha_{ij}\beta_{ij}\gamma_{ij})$
      $D_{ij} = (\sum_{f} \sum_{l=0}^{L} \sum_{m=-l}^{l} (c_{lf}^m(\alpha_{ij}\beta_{ij}\gamma_{ij}) - c_{lf_2}^m)^2)^{1/2}$
      if $D_{ij} \le D$ **then**
        $D = D_{ij}$
        $\mathbf{target} = \{c_l^m(\alpha_{ij}\beta_{ij}\gamma_{ij})\}$
      end if
    end for
  end for
  Appling the BFGS searching algorithm on the new parameter mesh generated by coefficients in **target**
  return the search result $\{\hat{c}_{l1}^m\}$
end

In the second step, we use the Broyden–Fletcher–Goldfarb–Shanno (BFGS) algorithm [12] to locally minimize (16) starting from the result of the first step. Because the result of the first step is already close to the target, this step generally needs only a few iterations. Although the dimension of the Jacobian matrix is large, the matrix is quite sparse. The computational time of this step is very low.

2) Fast Surface Alignment Algorithm: In the sampling-based search algorithm, if we do not want to miss the true global minimization, we need to use a large number n and a correspondingly small step size. Because the SPHARM coefficients must be calculated for every new Euler angles set (α, β, γ), the computational time is increased substantially with a larger n.

In order to reduce the computational complexity of search in Algorithm 2 [O(n^3)], we utilize the properties of the surface parameterization. There are north pole and south pole in every parameterized surface [3], and their movement follows the parameter mesh rotation on the surface. If the distance between two surfaces is minimal, their north/south poles are usually very close to each other in the object space. Therefore, in the first step, we align the surfaces' north poles and south poles by minimizing the value of

$$D_{\text{poles}} = \|v_1(0, \phi) - v_2(0, \phi)\| + \|v_1(\pi, \phi) - v_2(\pi, \phi)\|.$$

Based on the new north pole's position, we can search more carefully for the distance function minimum in its vicinity.

We still use the uniform sampling method in Algorithm 1 to generate the new north poles' position and the distance D_{poles} is calculated for each new north pole. In our implementation, we select the first ten promising positions (with the minimum D_{poles}) as the new north poles. For each new north pole, the parameter mesh is clockwise rotated to minimize the surface distance in (16). In the x-, y-, z-sphere coordinate systems, the north pole is mapped on $\hat{e}_3$, and thus, we have the new rotation matrix $R_{ZYZ}(\alpha\ \beta\ \gamma) = R_{ZYZ}(\alpha\ 0\ 0)^T$, $\alpha \in [0, 2\pi)$ and $R_{\text{obj}}(\alpha\,\beta\,\gamma) = R_{\text{obj}}(\alpha\,0\,0)^T$. In the second step, we use the same BFGS algorithm employed in Algorithm 2. Therefore, the computational complexity of the alignment algorithm is reduced to O(n^2).

III. Experiments and Discussions in Medical Image Analysis

The fast alignment algorithm for surface correspondence described before was used for shape analysis in selected medical image computing applications. Based on segmented MRI data of heart and brain, we use the SPHARM method to do surface reconstruction and apply the surface alignment algorithm presented in this paper to determine the correspondence between shapes. The established correspondence is necessary for researchers to perform comparative studies and access more functional details. In this section, we show how the surface alignment algorithm can help in these applications.

A. Comparison With the First-Order-Ellipsoid-Based Surface Alignment Method

In previous shape analysis study using the SPHARM description [4], researchers choose to use the three major axis of the first-order ellipsoid (which is computed from the first-order SPHARM coefficients) as the intrinsic coordinate system. Parameterization is rotated in the parameter space for normalization so that three main ridges of the first-order ellipsoid are moved to a canonical position [4], [5]. Their method works well if two or more objects have a similar orientation (e.g., aligning hippocampal shapes). However, this method may not work in some cases. The following is an example.

Fig. 3(a) and (c) shows the reconstructed surface of two ventricles of the heart (left ventricle and right ventricle). We separate the parameterization on the surface into eight regions using five lines ($\theta = \pi/2$ in white, north pole in yellow with $\theta = 0$, south pole in red with $\theta = \pi$, the other four lines represent $\phi = 0, \pi/2, \pi, 3\pi/2$). These five lines and two poles show the correspondence on the surfaces; thus, it can give us a visualized validation for the alignment result. The correspondence between surfaces in Fig. 3(a) and (c) are not established as the visualization shows. Fig. 3(b) and (d) shows their first-order ellipsoids. By using the previous method, the first-order ellipsoids and

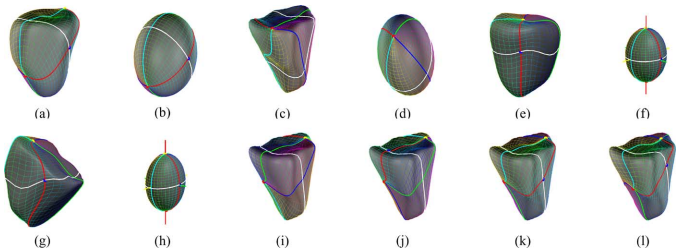

Fig. 3. Comparison of methods. (a) Reconstructed SPHARM surface of left ventricle. (b) First-order ellipsoid of surface (a). (c) Reconstructed SPHARM surface of right ventricle. (d) First-order ellipsoid of surface (c). By using the previous method, the first-order ellipsoids and parameterizations are rotated to the positions in (f) and (h), and the SPHARM surfaces and parameterizations are rotated as (e) and (g). (i) Result of poles alignment by using our algorithm. North (yellow point) and south (red point) poles are aligned close to the poles of (a). (i)–(k) Alignment procedure by rotating the parameter mesh along the north pole. For example, the red line is rotated from the back side (hidden) to the top side, and to the front side; the green line is rotated from the top side to the front side, and to the bottom side. (l) Last alignment result after using the BFGS algorithm in the second step.

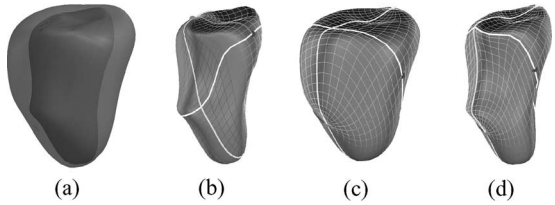

Fig. 4. (a) Visualization of the left ventricle without the parametric mesh. (b) Inner surface before alignment. (c) Outer surface that is fixed during alignment procedure. (d) Alignment result of inner surface.

TABLE I
END-DIASTOLIC WALL THICKNESS COMPARISON IN DIFFERENT DIRECTIONS OF LEFT VENTRICLE MEASURED BY 2-D, 3-D, AND PROPOSED METHODS

Location	Anterior			Septal			Lateral			Inferior		
Methods	2D	3D	Current	2D	3D	Current	2D	3D	Current	2D	3D	Current
Low (mm)	6.9	5.7	5.9	5.0	4.4	4.3	4.2	3.5	3.6	6.0	5.6	5.5
Mid (mm)	11.6	12.7	12.3	8.2	8.4	8.5	4.0	4.1	4.2	13.1	14.3	13.8
High (mm)	8.0	8.1	8.0	5.0	5.0	5.2	8.1	7.9	7.9	5.0	5.1	5.1

parameterizations are rotated to the positions in Fig. 3(f) and (h). Three main directions of the ellipsoids are moved to a canonical position. The regions with similar (θ, ϕ) values on two ellipsoids' surface are visualized by the same color. The surface correspondence is created when the first-order ellipsoid is aligned. As a result, the SPHARM surfaces and parameterizations should be rotated as Fig. 3(e) and (g). A limitation of this approach is that it cannot represent the real surface correspondence between two surfaces. The reason for this is that the left ventricle and right ventricle have two very different orientations of their first-order ellipsoid that are obvious in Fig. 3(b) and (d). Thus, although the first-order ellipsoids are rotated to the normalized positions, the surfaces are rotated to the opposite orientations.

Our new alignment algorithm produces a correct alignment in such cases, because it is a general surface alignment method that does not depend on any orientation information. Fig. 3(i)–(l) shows the results generated by our algorithm. Fig. 3(a) is the fixed surface and the parameterization in Fig. 3(c) is rotated to Fig. 3(l). The visualized color lines and poles can validate our result.

The effectiveness of our algorithm can also be validated by computing the surface correspondence distance defined in (16). The surface correspondence distance between surfaces in Fig. 3(e) and (g) is 258.6536 mm, but the surface correspondence distance between surfaces in Fig. 3(a) and (l) is 62.4798 mm. Our surface alignment algorithm generates a better result.

B. Surface Correspondence Alignment Between Epicardium and Endocardium

In [6], the SPHARM model is used to accurately measure and visualize heart and left ventricle geometry and function. Fig. 4(a) shows a visualization of the left ventricle without the parametric mesh. Two important parameters, the left ventricular wall thickness and wall stress, were accurately calculated using the SPHARM model. The new alignment algorithm in this paper can further simplify the measurement method; now, after aligning the surface correspondence between the left ventricular endocardial and epicardial surfaces, the wall thickness can be calculated simply as $\|v_{\text{endo}}(\theta_i, \phi_i) - v_{\text{epi}}(\theta_i, \phi_i)\|$, with (θ_i, ϕ_i) coming from the interesting region. Since the wall stress is related to wall thickness, we can also estimate it without placing additional efforts.

In cardiac MRI, since the positions and shapes of heart or ventricle comprise rich medical information, we cannot translate or rotate them in some heart functional analysis applications. For example, we can only align the surface correspondence between the endocardial and epicardial surfaces without any rotation or change on their shape if we want to accurately assess the changes in wall thickness. Our algorithm is suitable for this task.

Fig. 4(b) and (c) shows the results of SPHARM parameterization with unordered correspondence. We fix the epicardial surface and apply our algorithm on the endocardial surface. As a result, the parameterization is rotated to minimize the surface correspondence distance and the aligned result is shown in Fig. 4(d).

We compare the wall thickness results calculated by this simple method to the results from the 3-D measurement method proposed in [6] and the earlier method that makes measurement within a single imaging plane of short-axis MR images. Table I lists planar, 3-D, and proposed method measured wall thickness results in our experiments. We measure the planar (measured using ImageJ[2] from MRI 2-D slices), 3-D, and proposed method (by SPHARM model) of left ventricle wall thickness from the MRI of 20 pigs, and use their average measurements. Four normal directions are considered, and low section is close to apex of left ventricle, mid section is close to papillary muscles plane, and high section is close to the base of left ventricle. In the low part, the planar wall thicknesses overestimate the wall thickness [6], because the bias line is longer than the perpendicular line. The proposed method in this section can calculate the approximated wall thickness that are close to the result by using 3-D measurement method and does not overestimate the wall thickness at the apex of left ventricle like 2-D measurement method.

[2][Online]. Available: http://rsb.info.nih.gov/ij/

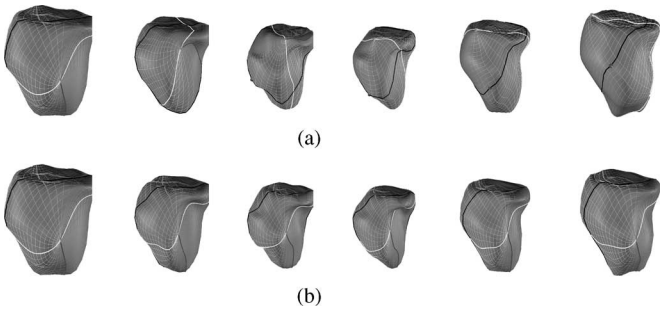

Fig. 5. (a) Sequence of a left ventricular inner surface during one heart cycle before surface alignment. (b) Surface sequence obtained after surface alignment.

C. Alignment for Spatiotemporal Cardiac Modeling

This new surface alignment algorithm also provides a promising method for studying spatiotemporal structures. In [13], surface tracking techniques (tracking points on 3-D shape using 2-D images) are used to create temporal sequence descriptions for points on the left ventricle inner surface through each heart cycle. Such temporal sequence descriptions can quantify the ventricular mechanical asynchrony or synchrony, which has important diagnostic and prognostic values, and can help determine optimal treatment in heart failures where a heart has a highly asynchronous contraction. Because the points are tracked on 2-D images and mapped to a 3-D surface, this method can only describe the heart contraction and dilation along the plane direction, and is not accurate for the perpendicular direction.

Combining the SPHARM description and our surface alignment methods offers a set of spatiotemporal surface correspondences for medical image analysis research. As in the previous example, our new algorithm generates more reasonable surface correspondences for the left ventricle sequence, and these surface correspondences describe the heart contraction and dilation in every direction of 3-D space. Based on this new model, more valuable diagnostic and prognostic information can be derived for helping make clinical determinations [14], [15].

Fig. 5(a) is a shape sequence of a left ventricular inner surface during one heart cycle. Before surface alignment, the correspondence between surfaces is not established. The shape sequence in Fig. 5(b) is the result after surface alignment. During the alignment procedure, each shape in the sequence is aligned with the first one.

D. Surface Registration for Hippocampal Shapes

The SPHARM description has been employed in several hippocampal shape discrimination studies. Davies *et al.* [16] combined the SPHARM description with a minimum description length model. Styner and Gerig [4] and Gerig and Styner [5] conducted a hippocampal shape classification study by using a SPHARM approach to calculate hippocampal asymmetry. In all the previous works, the first-order-ellipsoid-based method was used to finish the surface registration step. Since the first-order ellipsoid of a hippocampal shape is a real ellipsoid, using this ellipsoid for alignment often works well for hippocampal surfaces modeled by SPHARM. Here, we applied our surface registration method and compare it with the first-order ellipsoid SPHARM alignment method.

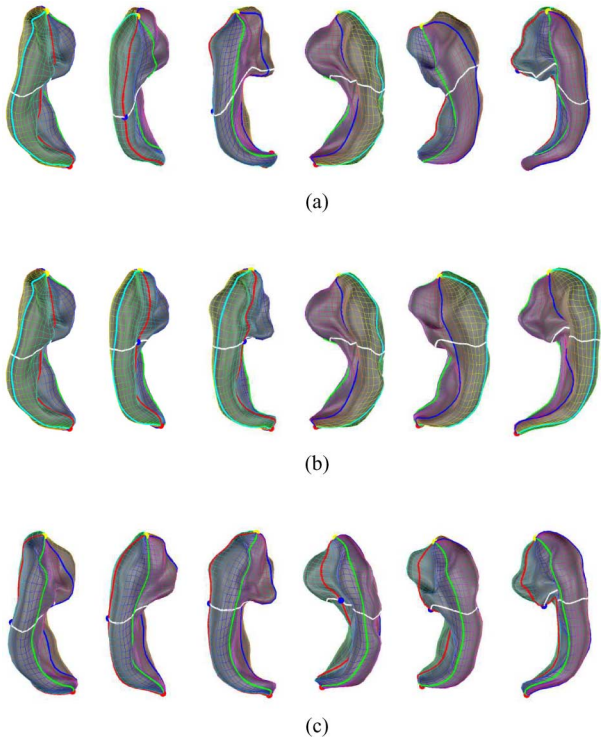

Fig. 6. Ten pairs of hippocampal shapes (left and right). (a) Three pairs of hippocampal shapes before surface registration. (b) Aligned results by using our method. (c) Aligned results by using the first-order-ellipsoid-based SPHARM alignment method. Same color is used to visualize points with the same (θ, ϕ) on different SPHARM shapes.

TABLE II
AVERAGE SURFACE DISTANCES COMPARISON OF ALIGNMENT RESULTS BETWEEN PREVIOUS METHODS AND OURS

Hippocampus	Left	Right
Our method	256.4950	233.3269
First order ellipsoid based method	348.9394	317.2034

In our experiments, ten pairs of hippocampal shapes (left and right) are used. Fig. 6(a) shows three pairs of hippocampal shapes before surface registration. Fig. 6(b) shows the aligned results by using our method, and meshes of the other hippocampal shapes are rotated to align with the first one. Fig. 6(c) shows the aligned results by using the first-order-ellipsoid-based SPHARM alignment method, and all the meshes of hippocampal shapes are rotated with the first-order ellipsoid alignment results. In the surface distances comparison, we calculated the surface distance between every object and the first one, and compared the average results. Our method outperforms the first-order ellipsoid alignment method (see also Table II). Thus, our surface registration method can get better alignment results even on the hippocampal shapes to which the first-order ellipsoid alignment method is often applicable.

IV. Conclusion

We have described a novel method for establishing surface correspondences between SPHARM parametric surfaces. In this method, we make use of the SPHARM rotational property to prove a parameterization rotation theorem that can help us rapidly rotate the SPHARM parameter mesh along the surface. The mean square distance between object surfaces is defined as the objective function. In the proposed surface distance minimization algorithm, we improve the computational complexity of the search algorithm from $O(n^3)$ to $O(n^2)$. Its efficacy is demonstrated in experiments based on several medical research problems, where we observe a significant improvement in robustness relative to existing shape modeling and analysis techniques.

References

[1] C. W. Chen, T. S. Huang, and M. Arrott, "Modeling, analysis, and visualization of left ventricle shape and motion by hierarchical decomposition," *IEEE Trans. Pattern Anal. Mach. Intell.*, vol. 16, no. 4, pp. 342–356, Apr. 1994.

[2] A. Matheny and D. B. Goldgof, "The use of three- and four-dimensional surface harmonics for rigid and nonrigid shape recovery and representation," *IEEE Trans. Pattern Anal. Mach. Intell.*, vol. 17, no. 10, pp. 967–981, Oct. 1995.

[3] Ch. Brechbühler, G. Gerig, and O. Kübler, "Parameterization of closed surfaces for 3D shape description," *Comput. Vis. Image Understanding*, vol. 61, no. 2, pp. 154–170, 1995.

[4] M. Styner and G. Gerig, "Three-dimensional medial shape representation incorporating object variability," in *Proc. IEEE Conf. Comput. Vis. Pattern Recognit.*, 2002, pp. 651–656.

[5] G. Gerig and M. Styner, "Shape versus size: Improved understanding of the morphology of brain structures," in *Proc. 4th Int. Conf. Med. Image Comput. Comput. Assisted Intervention*, LNCS 2208, 2001, pp. 24–32.

[6] H. Huang, L. Shen, J. Ford, F. Makedon, R. Zhang, and J. Pearlman, "Functional analysis of cardiac MR images using SPHARM modeling," *Proc. SPIE*, vol. 5747, pp. 1384–1391, 2005.

[7] P. J. Besl and N. D. McKay, "A method for registration of 3-D shapes," *IEEE Trans. Pattern Anal. Mach. Intell.*, vol. 14, no. 2, pp. 239–256, 1992.

[8] G. Burel and H. Hennocq, "Determination of the orientation of 3D objects using spherical harmonics," *Graph. Models Image Process.*, vol. 57, no. 5, pp. 400–408, 1995.

[9] G. S. Chirikjian and A. B. Kyatkin, *Engineering Applications of Noncommutative Harmonic Analysis: With Emphasis on Rotation and Motion Groups*. Boca Raton, FL: CRC Press, 2000.

[10] L. C. Biedenharn and J. C. Louck, *Angular Momentum in Quantum Physics*. Reading, MA: Addison-Wesley, 1981.

[11] D. W. Ritchie and G. J. L. Kemp, "Fast computation, rotation, and comparison of low resolution spherical harmonic molecular surfaces," *J. Comput. Chem.*, vol. 20, no. 4, pp. 383–395, 1999.

[12] R. Fletcher, *Practical Methods of Optimization*, 2nd ed. New York: Wiley, 1987.

[13] H. Huang, L. Shen, F. Makedon, S. Zhang, M. Greenberg, L. Gao, and J. Pearlman, "A clustering-based approach for prediction of cardiac resynchronization therapy," in *Proc. ACM Symp. Appl. Comput.*, 2005, pp. 260–266.

[14] H. Huang, L. Shen, R. Zhang, F. Makedon, B. Hettleman, and J. Pearlman, "A prediction framework for cardiac resynchronization therapy via 4D cardiac motion analysis," in *Proc. Int. Conf. Med. Image Comput. Comput. Assisted Intervention*, LNCS 3749, 2005, pp. 704–711.

[15] H. Huang, L. Shen, R. Zhang, F. Makedon, B. Hettleman, and J. Pearlman, "Cardiac motion analysis to improve pacing site selection in CRT," *J. Acad. Radiol.*, vol. 13, no. 9, pp. 1124–1134, 2006.

[16] R. H. Davies, C. J. Twining, P. D. Allen, T. F. Cootes, and C. J. Taylor, "Shape discrimination in the hippocampus using an MDL model," in *Proc. Int. Conf. Inf. Process. Med. Imaging*, LNCS 2732, 2003, pp. 38–50.

[17] S. E. Leicester, J. L. Finney, and R. P. Bywater, "A quantitative representation of molecular surface shape. I: Theory and development of the method," *J. Math. Chem.*, pp. 315–341, 1994.

Heng Huang (M'07) received the Ph.D. degree in computer science from Dartmouth College, Hanover, NH, in 2006.

He is currently an Assistant Professor in the Department of Computer Science and Engineering, University of Texas at Arlington. He is also the Director of the Biomedical Imaging and Visualization Laboratory. His current research interests include medical image analysis, computer vision, scientific visualization, and bioinformatics.

Li Shen (M'01) received the Ph.D. degree in computer science from Dartmouth College, Hanover, NH, in 2004.

He is currently an Assistant Professor in the Department of Computer and Information Science, University of Massachusetts Dartmouth, North Dartmouth. He also leads the Image and Pattern Analysis Laboratory. His current research interests include medical image analysis, geometric modeling, statistical shape analysis, data mining, biomedical imaging, and informatics.

Rong Zhang, photograph and biography not available at the time of publication.

Fillia Makedon received the Ph.D. degree in computer science from Northwestern University, Evanston, IL, in 1982.

In 2006, she joined the University of Texas at Arlington as the Jenkins Garret Chair and the Department Head of the Department of Computer Science and Engineering. She is the author of numerous research articles. She is the Editor of several journals.

Dr. Makedon is the recipient of the Senior Fulbright Award, and several NSF and other awards. She is also a member of numerous conference committees.

Andrew Saykin, photograph and biography not available at the time of publication.

Justin Pearlman, photograph and biography not available at the time of publication.